

Quantum interference control of free-carrier density in GaAs

J. M. Fraser* and H. M. van Driel†

Department of Physics, University of Toronto, 60 St. George Street, Toronto, Ontario, Canada M5S 1A7

(Received 10 April 2003; published 26 August 2003)

We have carried out theoretical and experimental investigations of optical phase controlled-free carrier injection in semiconductors via quantum interference between different absorption pathways connecting the same initial and final states in the valence and conduction bands. The interference schemes are theoretically modeled within a Fermi Golden rule approximation which also allows for a description in terms of the susceptibility formalism of nonlinear optics. Two different types of schemes involving interference between n and m multiphoton absorption events are considered depending on whether $n+m$ is even or odd. If $n+m$ is odd, phase control of carrier density can be observed only in a noncentrosymmetric crystal; if $n+m$ is even, interference can be observed in both centrosymmetric and noncentrosymmetric materials. The interference contribution to the density control is related to the imaginary part of the nonlinear electric susceptibility χ_{n+m-1} . Experimentally we have investigated carrier density control effects in GaAs at room temperature using nominally 150 fs optical pulses and considered an example for each of the two schemes: one-photon vs two-photon absorption with 0.775 and 1.55 μm pulses and one-photon vs three-photon absorption with 0.675 and 2.03 μm pulses. The main experimental features, including degree of phase control, are in good agreement with theory. We extract the relative magnitude of the imaginary and real components of χ_2 and χ_3 for GaAs at 1.55 μm and 2.03 μm , respectively.

DOI: 10.1103/PhysRevB.68.085208

PACS number(s): 78.47.+p, 42.65.-k, 78.55.Cr

I. INTRODUCTION

Laser control over electronic, atomic, and molecular phenomena has been pursued for several decades. Although laser intensity is often the defining optical parameter, it has also been recognized that the phase characteristics of one or more optical beams can also be used as control parameters. The operating principle is the manipulation of constructive and destructive interference in transition amplitudes to drive a system into states not achievable by more conventional means. This methodology has come to be referred to as coherent or quantum control. An early example of this approach was the control of optical absorption of a gas via interference of one- and three-photon absorption pathways using a fundamental and a derived third-harmonic optical pulses to connect the same initial and final states.¹ Since then, there have been numerous demonstrations of the use of phase-related optical pulses with commensurate frequencies to control systems with characteristically discrete states, e.g., manipulate the total yield of simple chemical reactions,² control semiconductor exciton population,³ or produce asymmetric ionization of carriers in quantum wells.⁴

For complex, e.g., polyatomic molecular, systems for which numerous pathways can connect the initial and final states and for which dephasing and redistribution of absorbed energy can occur rapidly, the use of well-defined, phase-related pulses with commensurate frequencies has produced limited successes. For such systems a more general approach in which pulse shapers are used to define phase and spectral characteristics of femtosecond pulses has been considered. The pulse shaper can be made to be part of a learning loop in which feedback from an experiment is used to define new pulse shapes, thereby eventually leading to a form of optimal control over a particular process through the myriad of quantum interference processes. These two differ-

ent approaches, sometimes referred to as interference and optimal control, are reviewed in the excellent papers of Shapiro and Brumer,⁵ and Rabitz *et al.*⁶

The control of continuum states or free carriers in a semiconductor may have been thought to be a candidate for optimal control. However, Atanasov *et al.*⁷ calculated that the interference between one- and two-photon absorption processes accessing valence- and conduction- band states in a bulk crystalline semiconductor could lead to the injection of an electrical current. Although this effect can occur in both centrosymmetric and noncentrosymmetric media, it was demonstrated in (noncentrosymmetric) GaAs at room temperature.⁸ Since current generation can occur for a broad range of continuum states, it should not be surprising that interference control would suffice to achieve this. More recently, we and our colleagues have also shown that interference between one- and two-photon absorption processes in GaAs can also lead to phase control of carrier populations or optical absorption.⁹ Due to parity selection rules, such an interference scheme is not allowed in a simple atomic system.

In this paper we report results of a theoretical and experimental investigation of how interference between transition amplitudes involving multiphoton absorption pathways using harmonically related beams can be used to control carrier density or net optical absorption in semiconductors and have carried out experiments in bulk GaAs at room temperature, in particular. Within the context of a Fermi's Golden rule formalism for absorption we show that if n is the number of photons involved in one pathway and m is the number of photons involved in the second, the control schemes can be divided into two general classes according to crystal inversion symmetry properties. If $n+m$ is odd, phase control of carrier density can be observed only in a noncentrosymmetric crystal; if $n+m$ is even, interference can be observed in

both centrosymmetric and noncentrosymmetric materials. An important component of this paper concerns the placement of the quantum interference process within the context of the standard macroscopic treatment of linear and nonlinear optics—the electric susceptibility formalism. The reason for this development is twofold. Inclusion of interference effects in Maxwell’s equations allows a full determination of the optical beams as they propagate through the sample. Thus, we can solve for the flow of energy between the beams and the material and the flow of energy between the beams themselves. This is important for the modeling of experimental results. In addition, consideration of quantum interference within the susceptibility formalism provides a new interpretation of the origins of certain tensor contributions to the optical response and their role in energy transfer between optical fields and semiconductor. For an $n+m$ scheme, the interference contribution to the density control is shown to be related to the imaginary part of the nonlinear electric susceptibility χ_{n+m-1} .

This paper is organized as follows. Section II describes a time-dependent perturbation theory analysis of quantum interference between interband transitions in a bulk semiconductor. This independent particle analysis details the microscopic origins of the effect. Since control of both the injected carriers and transmitted light beam is desired, propagation effects are modeled by solving the nonlinear coupled wave equations, derived from Maxwell’s equations including the nonlinear polarization terms associated with quantum interference. Insight is provided by a series expansion solution, appropriate in the thin sample limit. Section III describes the experimental techniques employed for the measurements on GaAs. The interference schemes considered here are one- and two-photon absorption (“1+2” scheme; optical pulses at wavelengths of 0.775 and 1.55 μm), and one- and three-photon absorption (“1+3” scheme; 0.667 and 2.03 μm) using nominally 150 fs optical pulses. Experimental results are described in Sec. IV. Comparison to theory is provided by a more complete modeling of the coupled nonlinear wave equations, solved by numerical simulation using a Green’s function formalism (Sec. V), and conclusions and comments on possible future work are included in Sec. VI.

II. THEORETICAL CONSIDERATIONS OF QUANTUM INTERFERENCE IN BULK SEMICONDUCTORS

A. Microscopic origins of quantum interference

We begin by considering absorption of light in a semiconductor crystal involving the promotion of an electron from a valence band to a conduction band using a Fermi Golden rule analysis. This section determines the expressions for the transition rate within the independent particle picture for a clean, cold semiconductor in the presence of two harmonically related beams which connect the same states in the conduction and valence bands. An electron of quasimomentum \mathbf{k} is treated independently of all other electrons. The response of the system to a perturbation arising from two or more beams with coherence times longer than the time scales of interest is determined by summing the contributions from all the electrons in the system, i.e., by summing over the

entire Brillouin zone. The independent particle picture analysis has been shown to be equivalent to a more detailed many-body formalism for expectation values of single-particle operators.^{10,11} Many-body effects (arising from excitons, other quasiparticles, or particle-particle scattering) are not considered and local-field corrections are also not included. These effects may play a role for experiments involving high carrier densities or carrier injection at energies in which Coulomb interactions are expected to play an important role (i.e., in GaAs, injection involving states within 5 meV of the bottom of the conduction band and the top of the valence band).

The theoretical development of quantum interference control for the 1+2 scheme was previously completed within a second quantization formalism.⁹ The independent particle picture, as employed here, is shown to yield the same results. In addition, the extension to a general $n+m$ scheme is straightforward in this formalism.

1. Fermi Golden rule calculation of linear and nonlinear absorption

In the independent particle picture, the optical properties of a semiconductor are determined by consideration of a single electron of quasimomentum \mathbf{k} , with Bloch state $|\Phi_v\rangle$ in band v . The states corresponding to energy levels at quasimomentum \mathbf{k} , in higher or lower bands provide a complete basis in which to understand the time development of the electron under a perturbation (involving negligible momentum transfer, i.e., within the dipole approximation). For a semiclassical analysis in which the material is treated quantum mechanically and the field classically, the Hamiltonian for one electron can be written as¹²

$$H = \frac{1}{2m} \left(\mathbf{p} - \frac{e}{c} \mathbf{A}(t) \right)^2 + U(\mathbf{r}), \quad (1)$$

where \mathbf{p} is the momentum operator, \mathbf{A} is the vector potential of the optical beam [$\mathbf{E} = -(1/c)(d/dt)\mathbf{A}$], and $U(\mathbf{r})$ is the periodic potential provided by the atomic lattice and other electrons in the system.¹³ As is the common practice, the interaction has been written in the velocity gauge [as opposed to the length gauge $\mathbf{rE}(t)$ where \mathbf{r} is the position operator] since Bloch states extend over the crystal. This Hamiltonian can be separated into unperturbed and perturbed contributions, where the perturbation arises from the light field [$-(e/mc)\mathbf{pA}(t)$]. The particle wave function can then be written in terms of a superposition of the basis set of the unperturbed system:

$$\psi(r,t) = \sum_j a_j(t) e^{-i\omega_j t} |\Phi_j\rangle,$$

where $|a_j(t)|^2$ corresponds to the probability of finding the electron in state j at time t . Application of time-dependent perturbation theory allows the determination of the coefficients a_j in terms of an order-expansion involving $a_j^{(q)}$, where q refers to the power dependence of the coefficient on electric field.

Initially, an optical beam with a single harmonic component at frequency ω is considered:

$$\mathbf{A}(t) = \mathbf{A}_\omega e^{-i(\omega+i\eta)t} + \mathbf{A}_\omega^* e^{i(\omega-i\eta)t},$$

where * indicates complex conjugate. The quantity η , which is small and positive, allows the optical fields to be turned on slowly in the distant past.¹⁴ The system of interest involves optical beams with wavelengths considerably longer than the length of a unit cell, thus justifying the dipole approximation. The system under study is a semiconductor at 0 K in which all the conduction bands are empty. For an electron initially in the valence band (state v), the first-order transition amplitude to conduction band state f is

$$a_f^{(1)}(t) = -\frac{e}{\hbar mc} \mathbf{p}_{fv} \mathbf{A}_\omega \frac{e^{-i(\omega-\omega_{fv}+i\eta)t}}{(\omega-\omega_{fv}+i\eta)}, \quad (2)$$

where

$$\mathbf{p}_{fv} = \langle \Phi_f | \mathbf{p} | \Phi_v \rangle, \quad \omega_{fv} = \omega_f - \omega_v.$$

The first-order expression also includes a nonresonant contribution related to $\mathbf{A}_{-\omega}$ that corresponds to emission. In the limit as η approaches zero, the one-photon absorption rate between states v and f is

$$\begin{aligned} T_f^{(1)}(\omega) &= \frac{d}{dt} |a_f^{(1)}|_{t=0}^2 \\ &= 2\pi \left(\frac{e}{\hbar mc} \right)^2 |\mathbf{p}_{fv} \mathbf{A}_\omega|^2 \delta(\omega - \omega_{fv}). \end{aligned}$$

The total one-photon absorption rate includes contributions from all the electrons in all the valence bands. Thus, the total transition rate is determined by summation over all possible initial and final states (including spins):

$$T^{(1)}(\omega) = 2\pi \sum_{\mathbf{k}, v, f} \left(\frac{e}{\hbar mc} \right)^2 |\mathbf{p}_{fv} \mathbf{A}_\omega|^2 \delta(\omega - \omega_{fv}). \quad (3)$$

For the purpose of clarity, the k dependence of \mathbf{p}_{fv} and ω_{fv} is not noted explicitly.

If the incident beam photon energy is less than the band-gap energy, the first-order term is zero and higher-order terms must be considered. Application of perturbation theory provides the amplitudes related to two- and three-photon absorption:

$$a_f^{(2)}(t) = \left(\frac{e}{\hbar mc} \right)^2 \sum_j \frac{[\mathbf{p}_{fj} \mathbf{A}_\omega][\mathbf{p}_{jv} \mathbf{A}_\omega]}{(\omega - \omega_{jv})} \frac{e^{-i(2\omega - \omega_{fv} + 2i\eta)t}}{(2\omega - \omega_{fv} + 2i\eta)}, \quad (4)$$

$$\begin{aligned} a_f^{(3)}(t) &= -\left(\frac{e}{\hbar mc} \right)^3 \sum_{l,j} \frac{[\mathbf{p}_{fl} \mathbf{A}_\omega][\mathbf{p}_{lj} \mathbf{A}_\omega][\mathbf{p}_{jv} \mathbf{A}_\omega]}{(\omega - \omega_{lv})(2\omega - \omega_{lv})} \\ &\quad \times \frac{e^{-i(3\omega - \omega_{fv} + 3i\eta)t}}{(3\omega - \omega_{fv} + 3i\eta)}. \end{aligned} \quad (5)$$

Intermediate states as denoted by j and l include the initial and final states. It should be noted that the higher-order terms as expressed here are not correct if lower-order terms are nonzero.¹² For instance, if the optical beam is one-photon resonant ($\omega = \omega_{fv}$), the second-order expression diverges when $j=f$. Since the present analysis considers only the first nonzero contribution to the transition amplitudes, these artificial divergences are not encountered. Equations (4) and (5) can be used to find two- and three-photon absorption rates in an analogous fashion to that used to obtain Eq. (3).

2. Quantum interference: 1+2 scheme

In the case for which the incident beam contains both fundamental and second-harmonic (SH) components and $\frac{1}{2}E_g < \hbar\omega < E_g$,

$$\begin{aligned} \mathbf{A}(t) &= \mathbf{A}_\omega e^{-i(\omega+i\eta)t} + \mathbf{A}_\omega^* e^{i(\omega-i\eta)t} + \mathbf{A}_{2\omega} e^{-i(2\omega+i\eta)t} \\ &\quad + \mathbf{A}_{2\omega}^* e^{i(2\omega-i\eta)t}, \end{aligned}$$

the transition rate between initial state v and final state f at quasimomentum \mathbf{k} is

$$T_f = \frac{d}{dt} [|a_f^{(1)}|^2 + |a_f^{(2)}|^2 + a_f^{(1)}(a_f^{(2)})^* + a_f^{(2)}(a_f^{(1)})^*]_{t=0}, \quad (6)$$

where the first-order term originates from the one-photon transition due to the SH beam and the second-order term is the two-photon transition related to the fundamental beam. The remainder of Eq. (6) is composed of cross terms between the individual amplitudes. As can be seen by inspection, the transition rate can be set to zero by careful selection of \mathbf{A}_ω and $\mathbf{A}_{2\omega}$; i.e., selecting appropriate phase and intensity values of the incident beams such that the cross terms cancel the one- and two-photon-absorption contributions. The second-order process usually requires a considerably more intense fundamental beam for this condition to be satisfied. Note also that Eq. (6) describes the transition rate for a single particle at a specific quasimomentum. The total transition rate must be determined considering all such particles. Setting the phase and intensity of the incident beams to provide perfect cancellation at one position in k space does not guarantee perfect cancellation over the entire Brillouin zone, as is described in more detail below. The full transition rate can be determined by substitution of Eqs. (2) and (4) into Eq. (6) and summing over the entire Brillouin zone and all possible bands:

$$T = 2\pi \sum_{\mathbf{k}, \nu, f} \left[\left(\frac{e}{\hbar mc} \right)^2 |\mathbf{p}_{f\nu} \mathbf{A}_{2\omega}|^2 + \left(\frac{e}{\hbar mc} \right)^4 \left| \sum_j \frac{[\mathbf{p}_{fj} \mathbf{A}_\omega][\mathbf{p}_{j\nu} \mathbf{A}_\omega]}{(\omega - \omega_{j\nu})} \right|^2 \right] \delta(2\omega - \omega_{f\nu}) - \left(\frac{e}{\hbar mc} \right)^3 [\mathbf{p}_{f\nu} \mathbf{A}_{2\omega}] \left(\sum_j \frac{[\mathbf{p}_{fj} \mathbf{A}_\omega][\mathbf{p}_{j\nu} \mathbf{A}_\omega]}{(\omega - \omega_{j\nu})} \right)^* + \text{c.c.} \quad (7)$$

The magnitude of the interference cross term can be calculated by fully evaluating this expression, but inspection yields some useful insight. For any material, time-reversal symmetry requires that $\omega_{j\nu}(\mathbf{k}) = \omega_{j\nu}(-\mathbf{k})$. In semiconductors with a center of inversion, $\mathbf{p}_{j\nu}(\mathbf{k}) = -\mathbf{p}_{j\nu}(-\mathbf{k})$ and can be considered purely real.¹⁵ Since the interference cross term in Eq. (7) is a product of an odd number of momentum matrix elements, it is odd in \mathbf{k} for centrosymmetric materials. As such, the relative phase of the interference term (as determined by the phases of the momentum matrix elements and the optical fields) at $+\mathbf{k}$ is always exactly π out of phase with the term at $-\mathbf{k}$. Summation over all \mathbf{k} space yields a zero result for the phase-dependent term, independent of the optical intensity or phases. Thus, the total carrier injection and optical absorption cannot be manipulated through the 1+2 scheme in centrosymmetric materials. In a noncentrosymmetric material, the interference term can have a component that is even in \mathbf{k} . Summation over all momentum space can yield a nonzero control of the total carrier injection rate, corresponding to a control of the effective transparency of the material. Note though that there is no requirement that the interference term be purely even in \mathbf{k} , thus in the general case, the relative phase of the interference term varies as a function of \mathbf{k} , causing a reduction in the possible control efficacy.

In addition to a reduction of control due to the k -space dependent relative phase, the ratio of the magnitudes of the one- and two-photon transition amplitudes also depends on \mathbf{k} . Thus, a ratio of fundamental and SH irradiances that provides perfect cancellation at \mathbf{k}_1 may not provide perfect cancellation at \mathbf{k}_2 . The analogy of the Michelson interferometer is useful in understanding how k -space variation of the relative phase and transition amplitude ratio limits the total contrast obtainable. For a single particle [Eq. (6)], balancing the arms (i.e., balancing the magnitude of one- and two-photon absorption) provides perfect contrast. The ensemble of particles corresponds to an interferometer involving many different paths. Variation of relative phase as a function of \mathbf{k} corresponds to a surface of one of the mirrors of the Michelson interferometer being uneven (Fig. 1— left). Controlling the overall path length difference cannot compensate for variations in individual paths. As a result the overall contrast as observed by the detector is reduced. The extreme limit occurs if the uneven mirror delays half of the beam by exactly π relative to the other half, reducing the contrast to zero. This corresponds to the case of the “1 + 2 matter interferometer” involving centrosymmetric materials. The second limiting factor, i.e., the k -space dependence of the ratio of transition amplitudes, can also be included in the Michelson analogy. This would correspond to a different reflection co-

efficient at different spatial points of one of the mirrors (Fig. 1— right). Changing the beam splitter ratio (like changing the ratio of fundamental to SH irradiance) may improve the fringe contrast but cannot completely compensate for a spatially inhomogeneous mirror. Unless the ratio of transition amplitudes has no dependence on \mathbf{k} , complete cancellation is not possible.

It is interesting to note that the result obtained for centrosymmetric materials, namely, that the cross terms at \mathbf{k} and $-\mathbf{k}$ have opposite signs, allows the production of bias-free currents. Due to this interference effect, more carriers are injected on one side of the Brillouin zone than the other. The resulting polar distribution in momentum space corresponds to a net motion of charge; this is the microscopic origin of the coherent control of current as described and observed by Haché,^{8,16} and others.^{17,18} The present analysis clearly shows the difference between the control of current and the control of carrier injection. Although both can be observed by the interference between one- and two-photon absorption, they have different material dependencies and the coherent control of current does not affect the total amount of light energy absorbed.

Equation (7) can be put into a more accessible notation with the total injected carrier density N and phase dependence explicitly noted. The total transition rate corresponds to three terms representing carrier injection originating from one-photon, two-photon, and cross-term contributions, respectively:

$$T = \dot{N}_{2\omega} + \dot{N}_\omega + \dot{N}_{\omega,2\omega}.$$

Substitution of $\mathbf{E}_\omega = (i\omega/c)\mathbf{A}_\omega$ and $E_\omega^i = |E_\omega^i|e^{i\phi_i}$ (the i th cartesian component of vector \mathbf{E}_ω), the interference term can be rewritten as

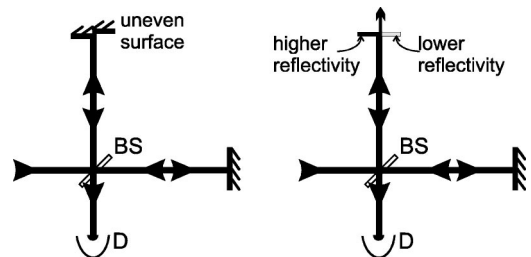


FIG. 1. Michelson interferometers that cannot achieve ideal fringe contrast due to variation in path length (left) and inhomogeneous reflectivity of one mirror (right). BS—beam splitter, D—detector.

$$\begin{aligned} \dot{N}_{\omega,2\omega} &= \xi_{2\omega}^{abc} E_{2\omega}^a E_{-\omega}^b E_{-\omega}^c + \text{c.c.} \\ &= 2 \xi_{2\omega}^{abc} |E_{2\omega}^a| |E_{-\omega}^b| |E_{-\omega}^c| \cos(\phi_{2\omega}^a - \phi_{-\omega}^b - \phi_{-\omega}^c), \end{aligned} \quad (8)$$

where repeated indices are summed over the Cartesian coordinates, and

$$\xi_{2\omega}^{abc} = \frac{\pi}{V} \frac{i}{\omega^3} \left(\frac{e}{\hbar m} \right)^3 \sum_{\mathbf{k},v,f,j} \left(\frac{p_{vf}^a [p_{fj}^b p_{jv}^c]}{\omega - \omega_{jv}} \right) \delta(2\omega - \omega_{fv}), \quad (9)$$

where V is the normalization volume. Note that the property that $\xi_{2\omega}^{abc}$ is purely real was used to obtain Eq. (8). This explicitly shows the phase dependence of the interference process and how it is related to the phases of the optical beams. For our purposes, the expression $\phi_{2\omega}^a - \phi_{-\omega}^b - \phi_{-\omega}^c$ is referred to as the phase parameter. As shown in Eq. (8), manipulation of the phase parameter provides dynamic control of the injected carrier rate.

3. Quantum interference: 1+3 scheme

It is clear that the previous analysis can be extended to higher-order interference schemes, involving n - and m -photon absorption, where $n\omega_a = m\omega_b$, $n\omega_a \hbar > E_g$, and n and m are positive integers. The form of the final term of Eq. (7) also suggests the material dependence for control of total carrier injection for these higher-order processes. When $n+m$ is odd, as is the case for 1+2 interference, the cross term is odd in \mathbf{k} for centrosymmetric materials, resulting in the control of total carrier generation dependent on the symmetry breaking of the material. For $n+m$ even, the cross term is expected to be even in \mathbf{k} for centrosymmetric materials. To verify this hypothesis, the interaction of a semiconductor with two beams of frequencies ω and 3ω is considered, where $\frac{1}{3}E_g < \hbar\omega < \frac{1}{2}E_g$.

The total transition rate is determined with the expressions for $a_f^{(1)}(t)$ [Eq. (2)] and $a_f^{(3)}(t)$ [Eq. (5)]:

$$T = 3\pi \sum_{\mathbf{k},v,f} \left[\left(\frac{e}{\hbar mc} \right)^2 |\mathbf{p}_{fv} \mathbf{A}_{3\omega}|^2 + \left(\frac{e}{\hbar mc} \right)^6 \left| \sum_{l,j} \frac{[\mathbf{p}_{fl} \mathbf{A}_{\omega}][\mathbf{p}_{lj} \mathbf{A}_{\omega}][\mathbf{p}_{jv} \mathbf{A}_{\omega}]}{(\omega - \omega_{jv})(2\omega - \omega_{lv})} \right|^2 \right] \delta(3\omega - \omega_{fv}). \quad (10)$$

$$+ \left(\frac{e}{\hbar mc} \right)^4 [\mathbf{p}_{fv} \mathbf{A}_{3\omega}] \left(\sum_{l,j} \frac{[\mathbf{p}_{fl} \mathbf{A}_{\omega}][\mathbf{p}_{lj} \mathbf{A}_{\omega}][\mathbf{p}_{jv} \mathbf{A}_{\omega}]}{(\omega - \omega_{jv})(2\omega - \omega_{lv})} \right)^* + \text{c.c.}$$

Note that for centrosymmetric materials, interference terms at \mathbf{k} and $-\mathbf{k}$ are equal. Thus the summation over all k space can result in a nonzero result.

With $\mathbf{E}_{3\omega} = (i3\omega/c)\mathbf{A}_{3\omega}$, the interference term in Eq. (10) can be put into more accessible notation:

$$\begin{aligned} \dot{N}_{\omega,3\omega} &= \xi_{3\omega}^{abcd} E_{3\omega}^a E_{-\omega}^b E_{-\omega}^c E_{-\omega}^d + \text{c.c.} \\ &= 2 \xi_{3\omega}^{abcd} |E_{3\omega}^a| |E_{-\omega}^b| |E_{-\omega}^c| |E_{-\omega}^d| \cos(\phi_{3\omega}^a - \phi_{-\omega}^b - \phi_{-\omega}^c - \phi_{-\omega}^d), \end{aligned} \quad (11)$$

where repeated indices are summed over the Cartesian coordinates and

$$\begin{aligned} \xi_{3\omega}^{abcd} &= \frac{-\pi}{V} \frac{1}{\omega^4} \left(\frac{e}{\hbar m} \right)^4 \sum_{\mathbf{k},v,f,l,j} \left(\frac{p_{vf}^a [p_{fl}^b p_{lj}^c p_{jv}^d]}{(\omega - \omega_{jv})(2\omega - \omega_{lv})} \right) \\ &\quad \times \delta(3\omega - \omega_{fv}). \end{aligned} \quad (12)$$

Since p_{lj}^a can be considered purely real for centrosymmetric materials, the required phase between the beams for maximum cancellation does not vary with \mathbf{k} in contrast to the results found for the 1+2 scheme. Maximum interference occurs at every \mathbf{k} for optical beams when $\phi_{3\omega}^a - \phi_{-\omega}^b - \phi_{-\omega}^c - \phi_{-\omega}^d = 0, \pi$. As found in the previous case, an intensity ratio that provides perfect cancellation at one position in k space does not guarantee perfect cancellation over the entire Brillouin zone. In the case where $3\hbar\omega$ is tuned to the band gap,

the wave functions for the relevant coupled valence- and conduction-band states possess atomic p - and s -type symmetries, respectively, in the absence of many-body corrections. In that case, as with the actual atomic case of population, one might expect the efficacy of control to approach unity.

B. Macroscopic interpretation of quantum interference

The origin of quantum interference in free carrier injection is easily understood in terms of the time-dependent perturbation analysis as outlined in the preceding section. This viewpoint is particularly well suited to understanding absorption at a specific location in the material but provides little information on the overall flow of energy between the beams themselves and between the beams and the crystal over some interaction length. To quantify these effects, it is convenient to place the quantum interference process into the context of the standard macroscopic phenomenological description of nonlinear optics—the nonlinear susceptibility formalism. This allows the modeling of energy flow and beam propagation through application of Maxwell equations. In addition to assisting in quantifying propagation effects, the determination of where this interference effect resides in the phenomenological model provides insight into the model itself. As developed in Ref. 9, the 1+2 interference term is related to the imaginary component of $\chi_2(-2\omega; \omega, \omega)$. A similar macroscopic analysis can be carried out for incident beams that

TABLE I. Phase-dependent modulation of the transmitted fundamental and SH beams and injected carrier density for 1+2 interference, to first order in z .

| χ_2 | $ E_\omega ^2$ | $ E_{2\omega} ^2$ | $- E_\omega ^2 - E_{2\omega} ^2$ |
|-----------|---|--|---|
| Complex | $-2 \chi_2 \sin(\Delta\phi^{(0)} + \phi_\chi)z$ | $2 \chi_2 \sin(\Delta\phi^{(0)} - \phi_\chi)z$ | $4\text{Im}\chi_2\cos(\Delta\phi^{(0)})z$ |
| Imaginary | $-2 \chi_2 \cos(\Delta\phi^{(0)})z$ | $-2 \chi_2 \cos(\Delta\phi^{(0)})z$ | $4 \chi_2 \cos(\Delta\phi^{(0)})z$ |
| Real | $-2 \chi_2 \sin(\Delta\phi^{(0)})z$ | $2 \chi_2 \sin(\Delta\phi^{(0)})z$ | 0 |

couple one- and three-photon transitions. Consider two beams of frequencies ω and 3ω , where $\frac{1}{3}E_g < \hbar\omega < \frac{1}{2}E_g$:

$$\mathbf{E}(t) = \mathbf{E}_\omega \exp(-i\omega t) + \mathbf{E}_{3\omega} \exp(-i3\omega t) + \text{c.c.}$$

Consideration of the energy loss from both beams permits the evaluation of the injected carrier density N :

$$\dot{N} = \dot{N}_\omega + \dot{N}_{3\omega} + \dot{N}_{\omega,3\omega}, \quad (13)$$

where the first two terms are the carrier injection rate due to three- and one-photon absorption processes, respectively, and the interference term is

$$\begin{aligned} \dot{N}_{\omega,3\omega} = & \frac{2}{\hbar} \text{Im}[\chi_3(-\omega; 3\omega, -\omega, -\omega) \mathbf{E}_{3\omega} \mathbf{E}_\omega \mathbf{E}_\omega \mathbf{E}_\omega] \\ & + \frac{2}{\hbar} \text{Im}[\chi_3(-3\omega; \omega, \omega, \omega) \mathbf{E}_\omega \mathbf{E}_\omega \mathbf{E}_\omega \mathbf{E}_{-3\omega}]. \end{aligned} \quad (14)$$

Similar to the symmetry properties of $\chi_2^{abc}(-2\omega; \omega, \omega)$,⁹ the interference term of Eq. (14) can be simplified by $\chi_3^{abcd}(\omega; -3\omega, \omega, \omega) = [\chi_3^{abcd}(-3\omega; \omega, \omega, \omega)]^*$ to be written as

$$\begin{aligned} \dot{N}_{\omega,3\omega} = & \frac{4}{\hbar} \text{Im}[\chi_3^{abcd}(-3\omega; \omega, \omega, \omega)] |E_{3\omega}^a| |E_\omega^b| |E_\omega^c| |E_\omega^d| \\ & \times \cos(\phi_{3\omega}^a - \phi_\omega^b - \phi_\omega^c - \phi_\omega^d), \end{aligned} \quad (15)$$

where repeated indices are summed. Not surprisingly, the presence of an interference term relies on a nonzero χ_3 tensor, a tensor that is nonzero even in centrosymmetric media. For zincblende materials, the nonzero elements are χ_3^{xxxx} , χ_3^{xyxy} , χ_3^{xyyx} , χ_3^{xyxx} and permutations arise from interchange of the x , y , and z coordinates. Application of intrinsic permutation symmetry and the symmetry of the $\bar{4}3m$ point group allows the determination of the sample orientation dependence of $\dot{N}_{\omega,3\omega}$ [for parallel polarized beams incident normally on a (100) zincblende material]:

$$\begin{aligned} \dot{N}_{\omega,3\omega} = & \frac{1}{\hbar} \text{Im}[3(\chi_3^{xxxx} + \chi_3^{xyxy}) + \cos(4\theta)(\chi_3^{xxxx} - 3\chi_3^{xyxy})] \\ & \times |E_{3\omega}| |E_\omega|^3 \cos(\phi_{3\omega} - 3\phi_\omega), \end{aligned} \quad (16)$$

where θ is the angle between the [001] axis and the direction of polarization.

As in the case of 1+2 interference scheme,⁹ energy transfer can occur between the two beams directly. For energy densities of the fundamental and third-harmonic beams (ϵ_ω and $\epsilon_{3\omega}$), the rate of energy transfer is

$$\begin{aligned} \dot{\epsilon}_{3\omega} - \dot{\epsilon}_\omega = & 4(3\omega) \text{Re}[\chi_3^{abcd}(-3\omega; \omega, \omega, \omega)] \\ & \times |E_{3\omega}^a| |E_\omega^b| |E_\omega^c| |E_\omega^d| \\ & \times \sin(\phi_{3\omega}^a - \phi_\omega^b - \phi_\omega^c - \phi_\omega^d). \end{aligned} \quad (17)$$

Due to propagation effects, this phase-dependent term also contributes to the carrier injection rate through variation of the one-photon absorption term primarily.

C. Propagation effects

Since phase-dependent modifications to the injected carrier density from energy transfer between the beams arise from two optical processes cascaded in series, analysis of this effect requires consideration of the propagation of the beams in the semiconductor. Due to their cascaded nature, the change to carrier injection dependent on $\text{Re}\chi_{2(3)}$ and $\text{Im}\chi_1$ is expected to have a higher-order dependence on interaction length compared to carrier injection from $\text{Im}\chi_{2(3)}$. A coupled wave analysis (derived from Maxwell's equations) for our single- and higher-harmonic beams in a semiconductor slab quantifies the various contributions to carrier injection. Two approaches were used to solve this problem. An analytic approximation involving a series solution was used to provide insight into the various contributions. To avoid assumptions necessary in the series solution, the system was modeled with a Green's function formalism and solved numerically. This was required for the analysis of experimental results as described in Sec. V.

The coupled Maxwell's equations, including nonlinear source terms, are simplified using the slowly varying envelope approximation and by setting the phase mismatch to zero. The quantities that are obtained are the amplitudes of the electric-field envelopes for both the fundamental and higher-harmonic fields, and the phase parameter as a function of sample depth (z). The phase dependence to first order in z is summarized in Tables I and II for different values of the phase of $\chi_{2(3)}$ (ϕ_χ). The variable $\Delta\phi^0$ corresponds to the value of the phase parameter at $z=0$. The fourth column indicates the phase dependence of carrier injection (provided by energy conservation). Two specific values of ϕ_χ are con-

TABLE II. Phase-dependent modulation of the transmitted fundamental and TH beams and injected carrier density for 1+3 interference, to first order in z .

| χ_3 | $ E_\omega ^2$ | $ E_{3\omega} ^2$ | $- E_\omega ^2 - E_{3\omega} ^2$ |
|-----------|---|--|---|
| Complex | $-2 \chi_3 \sin(\Delta\phi^{(0)} + \phi_\chi)z$ | $2 \chi_3 \sin(\Delta\phi^{(0)} - \phi_\chi)z$ | $4\text{Im}\chi_3\cos(\Delta\phi^{(0)})z$ |
| Imaginary | $-2 \chi_3 \cos(\Delta\phi^{(0)})z$ | $-2 \chi_3 \cos(\Delta\phi^{(0)})z$ | $4 \chi_3 \cos(\Delta\phi^{(0)})z$ |
| Real | $-2 \chi_3 \sin(\Delta\phi^{(0)})z$ | $2 \chi_3 \sin(\Delta\phi^{(0)})z$ | 0 |

sidered. For χ purely imaginary (i.e., $\phi_\chi = \pi/2$), the envelopes are in phase and the carrier injection is π out of phase. The interference in carrier injection affects both beams in the same way. The only modification to the pump intensities is due to enhanced or suppressed absorption. For χ_2 purely real (i.e., $\phi_\chi = 0$), the quantum interference contribution is null and there is no phase-dependent change to carrier injection. Changes to the pump intensities are due solely to energy transference between the two beams; the electric-field envelopes are π out of phase. Cascaded effects ($\text{Re}\chi_{2(3)}$ followed by $\text{Im}\chi_1$) do not appear until second order in z . These results suggest an interesting application: experimental measurement of the phase offset value provides an indicator of the ratio of $\text{Re}\chi_{2(3)}$ to $\text{Im}\chi_{2(3)}$, i.e., the phase of $\chi_{2(3)}$.

III. EXPERIMENTS

The apparatus used for the study of the 1+3 scheme is illustrated in Fig. 2. The 1+2 apparatus was described previously.⁹ For both studies, all optical beams originated from an optical parametric amplifier (OPA), pumped by a regeneratively amplified titanium-doped sapphire laser, described elsewhere.^{19,20} Optical pulses are produced by the OPA at a repetition rate of 250 kHz. Fundamental beams

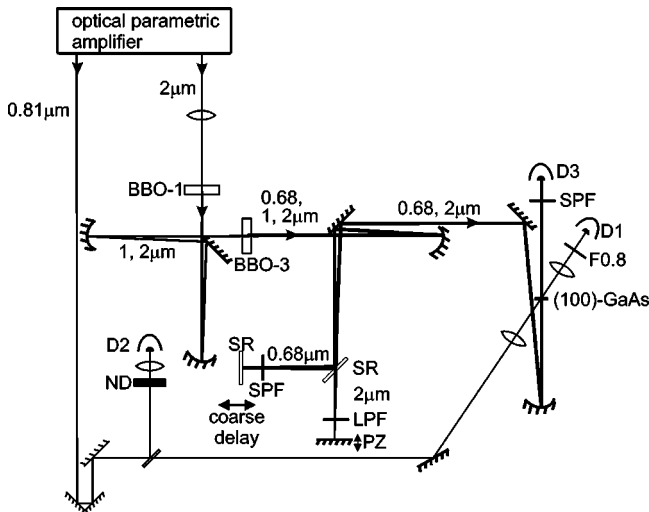


FIG. 2. Experimental apparatus used for 1+3 studies. BBO-1—SH generation crystal, BBO-3—sum-frequency generation crystal, LPF—long wavelength pass filter, SPF—short wavelength pass filter, ND—neutral density filter, PZ—piezoelectric controlled mirror, SR—dielectric to reflect short wavelengths and transmit long wavelengths, $D1$, $D2$, $D3$ —silicon detectors, and $F0.8$ — $0.8 \mu\text{m}$ notch filter.

centered at $1.55 \mu\text{m}$ and $2.03 \mu\text{m}$ (time-bandwidth products of 0.6 and 1.0, pulse durations of 120 and 170 fs respectively) were used for the two studies. Phase-locked and harmonically related beams were produced by nonlinear mixing in birefringent crystals. For the 1+3 studies, third harmonic (TH) of the fundamental beam could not be efficiently generated directly. The TH beam was produced through second-harmonic generation of the fundamental beam [1 mm thick β -barium borate (BBO), type I mixing: $o+o \rightarrow e$, $\theta_{pm} = 21.3^\circ$], followed by sum-frequency mixing $\omega+2\omega \rightarrow 3\omega$ (3 mm thick BBO, type II mixing: $e+o \rightarrow e$, $\theta_{pm} = 24.7^\circ$). The SH beam was later removed by filtering. To minimize phase distortion between the beams, manipulation of the beams was done with reflective optics and the use of transmission optics was kept to a minimum.

Phase control between the two beams is accomplished with a two-color Michelson interferometer. The two beams are separated by a dichroic mirror. Leakage between the two arms was avoided by transmission filters and dielectric mirrors. Fine control of one delay line (provided by a mirror mounted on a piezoelectric [PZ] actuator) relative to the other allows control of the phase between the two beams. Background-free phase-dependent measurement was accomplished by lock-in detection synchronized to the fast motion of the PZ actuator, controlled by a function generator. The controller and PZ stage used could dither submicron distances at a rate of 1 kHz. The robustness of this detection scheme to noise is a key advantage of this design. Computer interfacing and control allowed automation of the measurement procedure. The control program created a slowly ramping signal that was added electronically to the function generator output wave form and input to the PZ controller. The resulting motion caused the PZ to dither by an amplitude determined by the function generator while sweeping through a slowly varying offset.

The two-color interferometer required careful alignment to ensure a constant value for the phase parameter of the profile of the beams. Alignment for the 1+3 procedure used the interference process itself. The nonlinear optical mixing process causes a phase-dependent variation of transmitted TH power. The resulting TH profile after the (100)-GaAs sample was imaged by a quadrant detector consisting of four independent detectors. Even though the phase-dependent variation of the transmitted beam was small, lock-in amplification allowed it to be resolved. Noncollinear beams (i.e., fringes in the spatial mode) result in phase offsets between the four signals. The interferometer alignment was varied until all four traces were synchronized, corresponding to a single fringe present in the far-field mode. Single fringe alignment was verified by rotating the quadrant detector by 45° and ensuring no loss of trace synchronization.

TABLE III. Samples characteristics

| Study | Orientation | Thickness (μm) | Wavelengths (μm) | Coh. length $l_{coh} =$ | l_{coh} (Ref. 22) (μm) | l_a (Ref. 22) (μm) |
|-------|-------------|--------------------------------|----------------------------------|--|--|--------------------------------------|
| 1+2 | (111) | 0.65 | 0.775/1.55 | $\frac{c}{2(2\omega)(n_{2\omega}-n_\omega)}$ | 1.2 | 1.4 |
| 1+3 | (100) | 0.20 | 0.675/2.03 | $\frac{c}{2(3\omega)(n_{3\omega}-n_\omega)}$ | 0.75 | 0.61 |

Due to the different material symmetry dependencies of the two interference schemes, two sample orientations of GaAs were used: (100) and (111). For normal incidence beams (100) GaAs was sufficient for the 1+3 studies. The 1+2 studies, which exploited the nonzero χ_2^{xyz} tensor element, could not use (100) orientation with normal incidence beams. Non-normal incidence beams could have provided a nonzero projection of the electric fields on the xyz tensor element in a (100)-orientation sample but this experimental geometry is not practical. Dispersion would require the two beams to be set incident at different external angles to match internal angles. In addition, the high index of GaAs causes the internal angle in the material to be relatively small for even large external angles. For these reasons, normal incidence beams and (111) GaAs were used for the 1+2 studies.

Since both samples were grown by molecular beam epitaxy, thin samples could be produced. Sample length was set taking absorption and coherence lengths into consideration. The absorption depth of interest (l_a) is the sample length for the *electric field* to fall to $1/e$ of its incident value, which is twice the absorption depth of the intensity. The coherence length l_{coh} is limited due to dispersion between the two optical beams in the material and is defined as the crystal length required for the phase parameter to vary by π , i.e., the interference varies from constructive to destructive over the interaction length. The sample length was chosen to maximize the total number of carriers affected by the phase-dependent process.²¹ This corresponds to an interaction length approximately half of the coherence length. The 1+3 sample was designed with a shorter length due to the short absorption depth of the TH electric field. For the sample lengths used (Table III), phase mismatch did not drastically decrease control efficacy. The reduction in efficacy due to phase mismatch is estimated to be $\approx 12\%$ in the 1+2 studies and 3% in the 1+3 studies.²¹ The sensitivity of the carrier monitoring technique is also related to sample length as discussed below.

Carrier density was monitored by probing the sample with a separate optical beam. Since experiments were performed in thin samples, carriers could be monitored by the transmission of a probe beam whose photon energy was larger than the material band gap.²³ State filling was the dominant cause of transmission change for the probe wavelengths and carrier densities used in these studies.²⁴ The probe absorption is reduced due to an increase in the occupation factors of the electron and hole states (f_e and f_h) involved with the transition, according to $\alpha = \alpha_0(1 - f_e - f_h)$ where α_0 is the quiescent absorption of the material.²⁵ For a small change in

absorption, $\Delta\alpha$, the change in transmission through a sample of length l is $\Delta T_{probe}/T_{probe} = -\Delta\alpha l$ where $\Delta T_{probe} = T_{probe}(N) - T_{probe}$ and $T_{probe}(N)$ is the fraction of probe power transmitted through the sample for an injected carrier density of N [$T_{probe}(0)$ is written as T_{probe}]. To maximize the sensitivity of the measurement process, the independent probe beam was selected to have a lower photon energy than the one-photon resonant pump beam, and thus it monitored states close to the bottom of the band. Thermalization of the injected carriers causes these states to be occupied after a few picoseconds after injection. This method has three distinct advantages:

(i) The transmitted pump beams can be removed after the sample by wavelength filtering without affecting the probe beam.

(ii) The density of states at the bottom of the band is lower thus the change in absorption is larger for a given density of carriers.²⁶

(iii) The thermalization of the carrier population into an Fermi-Dirac distribution will cause the lower states to be filled at the expense of the higher states.

To verify the linearity of the probe transmission as a function of carrier density at this wavelength, the probe time delay was set to 4 ps and ΔT_{probe} was monitored as a function of one-photon resonant pump beam irradiance, over more than two orders of magnitude of carrier density (Fig. 3). The delay of 4 ps was chosen to allow the injected carri-

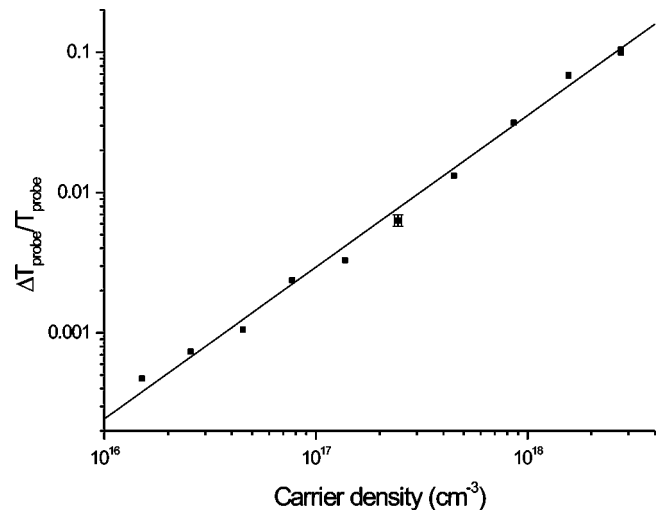


FIG. 3. Change in transmitted $0.83\text{-}\mu\text{m}$ probe as a function of injected carrier density in (111)-GaAs sample. The solid line is a best fit to the data.

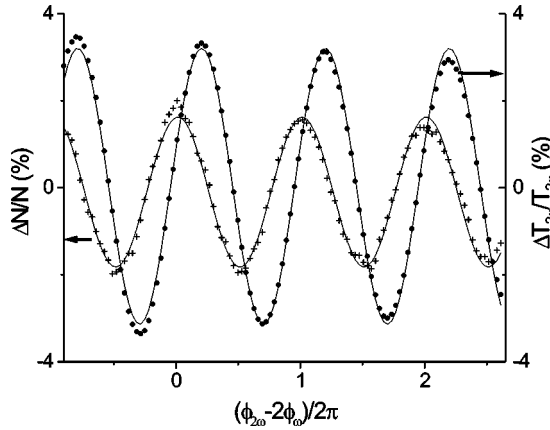


FIG. 4. Phase-dependent change to carrier injection (+) and transmission of the SH beam (●). The solid traces are sinusoidal fits to the data.

ers to thermalize and occupy the states at the bottom of the band. A fit of this data with two parameters (A and B) according to $\Delta T = AI^B$ gives a value of $B = 1.08 \pm .03$ which is not far from the expected value of unity.

The above discussion is concerned with maximizing the change to the absorption coefficient α for a given carrier density. Probe sensitivity is also improved if the change in transmission of the probe beam [$I_{probe}(z)$] is maximized for a given change to the absorption coefficient. Assuming a uniform change to the absorption coefficient over the sample length, the preferred probe interaction length is found by maximizing $(d/d\alpha)I_{probe}(0)e^{-\alpha z}$. From these considerations, the ideal sample length is the probe beam absorption depth. This interaction length is close to the optimum sample length as determined above for the 1+2 studies. The 1+3 sample was more tightly constrained by the previous considerations of coherence length and the absorption depth of the TH electric field.

IV. EXPERIMENTAL RESULTS

Preliminary results for the 1+2 interference scheme were described previously.⁹ Carrier injection and optical transmission were controlled through the phase parameter (Fig. 4). Rotation of the (111)-GaAs sample on an axis parallel to the beam wave vectors allowed the mapping of the modulation amplitude as a function of crystal orientation (Fig. 5). Change of orientation varies the projection of the electric-field polarizations on χ_2 . The sample orientation is characterized by the angle (θ) between $\mathbf{E}_{2\omega}$ and the $[01\bar{1}]$ axis of the semiconductor. The peak in the trace corresponded to the fundamental beam polarization aligned to the $[01\bar{1}]$ direction. In addition to the magnitude of the modulation, there is information contained in the relative phase of the modulation trace. For instance, traces measured at sample orientations of $\theta=30^\circ$ and $\theta=90^\circ$ were π out of phase. This information was included in Fig. 5 by the sign assigned to the amplitude. The solid curve is a best fit to the function $\sin(C\theta)$, with $C = 2.9 \pm .05$; this is close to the value of 3 predicted by material symmetry properties.

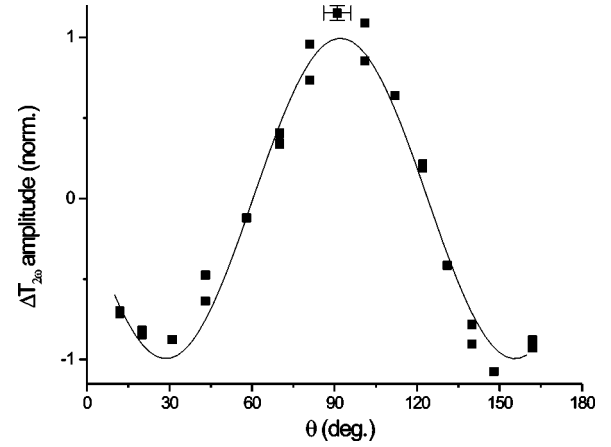


FIG. 5. SH transmission modulation amplitude as a function of sample rotation (θ). The solid trace is a sinusoidal fit to the data.

In the 1+3 scheme, a fundamental beam at $2.03 \mu\text{m}$ and TH beam at $0.675 \mu\text{m}$ were focused on the (100)-GaAs sample with beam waists of $35 \pm 2 \mu\text{m}$ and $54 \pm 2 \mu\text{m}$ (measured by the knife-edge technique). Peak irradiances were 2.1 GW/cm^2 and 90 MW/cm^2 , respectively. The modulations of the transmitted TH pump beam and injected carrier density were simultaneously monitored as a function of phase (Fig. 6). The carrier modulation amplitude was slightly larger than 0.1% of the total number of carriers injected and the change in TH transmission was slightly larger than 0.3%. This is not the maximum modulation amplitude possible for this interference scheme since the two injection processes (from one- and three-photon absorption) are not balanced at these irradiances. This is discussed in more detail below. In Fig. 6, the peak in carrier injection was assigned a relative phase of zero since the absolute value for the phase parameter was not experimentally determined. The phase offset between these two curves is 0.18π with a standard deviation of 0.06π .

For the irradiances used above, the number of carriers due to one-photon absorption dominated over the quantity injected by three-photon absorption. For a fundamental beam

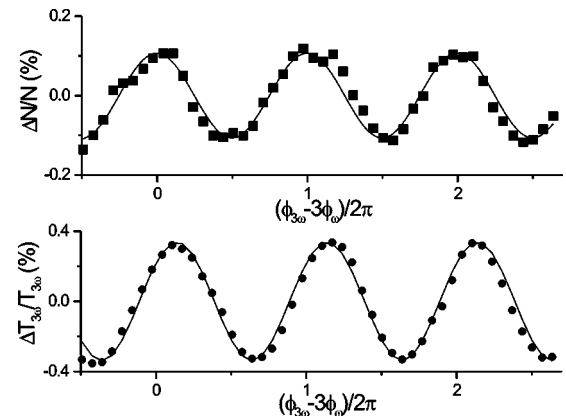


FIG. 6. Phase-dependent change to carrier injection (■) and transmission of the TH beam (●). The solid traces are sinusoidal fits to the data.

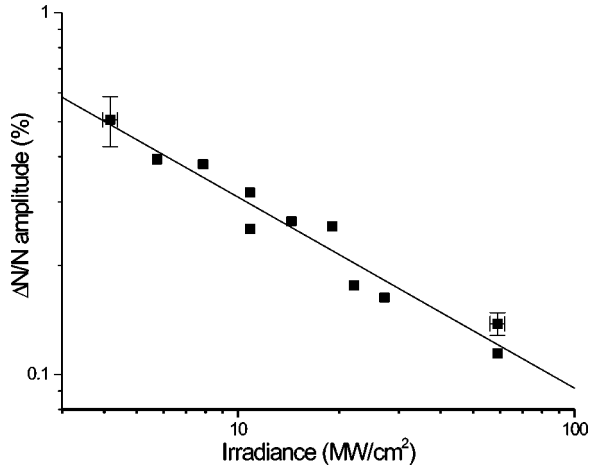


FIG. 7. Phase-dependent modulation amplitude of injected carriers as a function of TH beam irradiance. The solid trace is a best fit to the data.

irradiance of 2.1 GW/cm², a reduction in the TH irradiance reduced the difference between the two injection rates (Fig. 7). The efficacy of the control process improved for lower TH irradiances but did not reach a plateau. Below a TH beam irradiance of 4 MW/cm², the probe phase-dependent modulation is obscured by background noise. As described by Eq. (13) (for a constant fundamental beam irradiance), the data in Fig. 7 are expected to fit a relationship of the form:

$$\frac{\Delta N}{N} = \frac{DI_{3\omega}}{N_{\omega} + N_{3\omega}},$$

where N_{ω} ($N_{3\omega}$) is the number of carriers injected by the three- (one-) photon absorption processes, $I_{3\omega}$ is the TH beam irradiance, and D is a fitted constant. The solid line in Fig. 7 is a fit to the exponential function $\Delta N/N = AI_{3\omega}^B$ with $B = -0.53 \pm 0.04$. This is consistent with the value of $\Delta N/N$ being dominated by one-photon absorption. The density of carriers injected by one-photon absorption at the lowest measurable irradiance was $4 \times 10^{16} \text{ cm}^{-3}$.²² For a three-photon absorption coefficient of $0.14 \text{ cm}^3/\text{GW}^2$,²⁷ and a fundamental irradiance of $2 \text{ GW}/\text{cm}^2$, the carrier density injected by the three-photon process is calculated to be $3 \times 10^{14} \text{ cm}^{-3}$. Even though measurements at such low carrier densities could not be made, an estimate of the maximum fringe contrast can be obtained by extrapolating the trace shown in Fig. 7 to lower TH irradiances. For a three-photon absorption coefficient of $0.14 \text{ cm}^3/\text{GW}^2$, the maximum modulation amplitude is 3.3% of the total number of injected carriers. As noted earlier, the modulation amplitude is expected to be larger for control involving states close to the bottom of the band, but this could not be experimentally verified due to the limited tuning range of the OPA.

The effect of chirp on the phase-dependent modulation was investigated by introducing additional glass in the beam path. The modulation envelope did not change, although the overall magnitude decreased. The information contained in the modulation envelope is similar to that provided by an

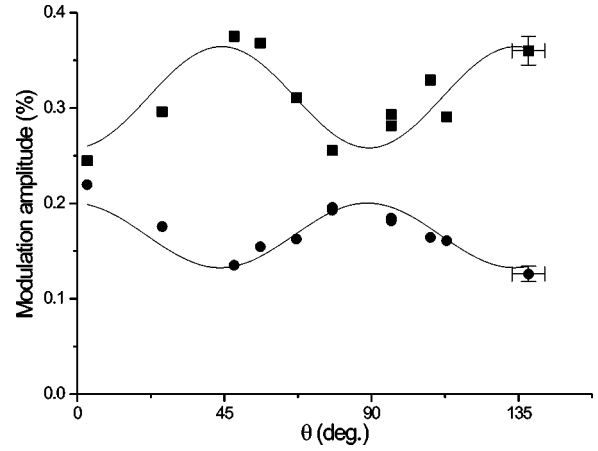


FIG. 8. Modulation amplitude of $\Delta T_{3\omega}/T_{3\omega}$ (■) and $\Delta N/N$ (●) as a function of (100)-GaAs orientation. The solid traces are sinusoidal fits to the data.

interferogram obtained from a one-color interferometer, namely, the power spectrum of the beam. Since even an incoherent light source can produce an interferogram, any light beam can produce the quantum interference effects under study. Although this is technically true, chirp does reduce the amplitude of the envelope by reducing the efficiency of the nonlinear process. This is analogous to changing the beam splitter ratio in the one-color interferometer from a 50:50 value. The envelope shape and oscillation period do not change but the fringe contrast is reduced. In a similar fashion, an incoherent light source would produce a negligible quantum interference effect of the type discussed in this paper.

The modulation amplitude for both carrier density and transmitted pump beam was shown to agree with the four-fold symmetry of the crystal structure (Fig. 8). Unlike the results for the 1+2 interference scheme, sample rotation permits access to different tensor contributions [Eq. (16)]. The sample orientation angle θ refers to the angle between the polarization of the pump beams and the [001] crystal axis. The modulation amplitudes have different dependencies on the sample orientation. These results would not be obtainable if only the cascaded process was involved, since then a maximum modulation amplitude in the transmitted TH pump beam would correspond to a maximum modulation in injected carriers. An intuitive understanding of these results can be obtained by consideration of the coupled wave equations in the thin sample limit. Within this model, the phase-dependent transmitted TH power depends on $|\chi_3(-3\omega; \omega, \omega, \omega)|$ while the change in injected carriers depends on $\text{Im}\chi_3(-3\omega; \omega, \omega, \omega)$ (Table II). From Eq. (16), the effective χ_3 elements at 0° and 45° are χ_3^{xxxx} and $\frac{1}{2}(\chi_3^{xxxx} + 3\chi_3^{xyyy})$, respectively. The results of Fig. 8 are then consistent with the magnitude of $2\text{Im}\chi_3^{xxxx}$ being greater than the magnitude of $\text{Im}[\chi_3^{xxxx} + 3\chi_3^{xyyy}]$ but $2|\chi_3^{xxxx}| < |\chi_3^{xxxx} + 3\chi_3^{xyyy}|$. The semi-*ab initio* calculations by Moss *et al.*²⁸ predict values of the tensors elements for $2.03 \mu\text{m}$ light that agree with these inequalities.

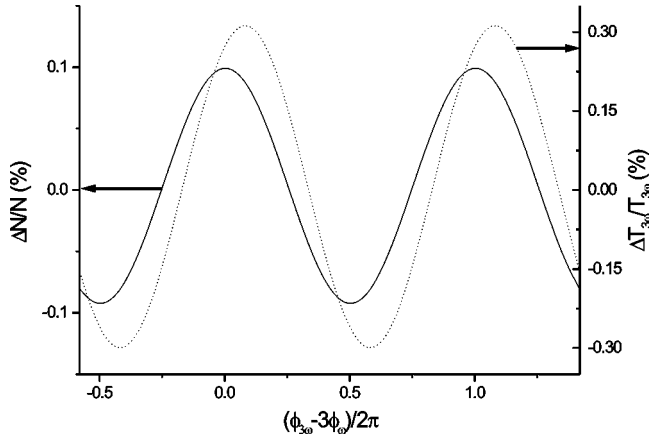


FIG. 9. Injected carrier density (solid line) and transmitted TH power (dotted line) as a function of the phase parameter in (100) GaAs.

V. ANALYSIS

To interpret the experimental results, the nonlinear mixing and free carrier injection processes occurring in the thin samples are modeled more completely than the series solution described in Sec. II. To relax the assumptions inherent to the series solution, a more detailed analysis involving a numerical simulation is required. The simulation solves for the self-consistent carrier density, electric-field amplitudes, and phases as a function of crystal position using a Green's function formalism. This analysis includes several processes that were neglected in the series solution. Not only is the thin interaction length assumption not made, but phase mismatch and reflections from boundaries are also included. Phase mismatch arises due to dispersion between the fundamental and higher-harmonic beams. In addition, the coupled wave analysis assumed that all beams were propagating in one direction even though electric fields from the polarization source terms propagate in all directions. This approximation is usually appropriate since phase mismatch in sufficiently long samples renders the backward propagating beams negligible. This is not a good assumption for interaction lengths on the order of

TABLE IV. Properties of incident light fields and (100)-GaAs sample as modeled by 1+3 numerical simulations, unless otherwise noted.

| Parameter | Value |
|--|---|
| Fundamental wavelength | 2.03 μm |
| Fundamental irradiance | 2.1 GW/cm^2 |
| TH irradiance | 0.09 GW/cm^2 |
| GaAs n_ω | 3.34 (Ref. 22) |
| GaAs $n_{3\omega} + i\kappa_{3\omega}$ | 3.8 + 0.17i (Ref. 22) |
| Sapphire n_ω | 1.7 |
| Sapphire $n_{3\omega}$ | 1.7 |
| χ_3 | $-(1.4 + 0.14i) \times 10^{-18} \text{ m}^2/\text{V}^2$ |
| $\text{Im}\chi_5$ | $4.7 \times 10^{-36} \text{ m}^4/\text{V}^4$ (Ref. 27) |
| Sample length | 0.20 μm |
| Pulse duration | 170 fs |

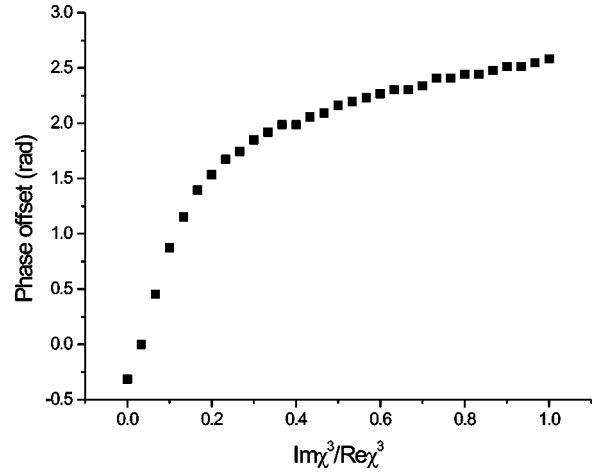


FIG. 10. Phase offset between carrier density and transmitted TH traces as a function of $\text{Im}\chi_3/\text{Re}\chi_3$ in (100) GaAs for normally incident beams.

the wavelength. The numerical model does not invoke this assumption.

The main challenge in determining a solution for this system is that the electric-field amplitudes depend on the polarization source terms which themselves depend on the fields. Since counterpropagating beams are present, this problem cannot be solved simply by following the propagation of the optical beams through the crystal. For instance, complete knowledge of the incident beams is not sufficient information to know the electric-field density at the entrance face due to its dependence on the polarization source terms throughout the material. An iterative process was implemented to obtain a self-consistent solution.

Similar algorithms were implemented for both the 1+2 and 1+3 studies. The later is described here and results from both schemes are summarized. The simulation included nonlinear source terms originating from $\text{Re}\chi_3(-3\omega; \omega, \omega, \omega)$, $\text{Im}\chi_3(-3\omega; \omega, \omega, \omega)$, and $\text{Im}\chi_5(-\omega; \omega, \omega, \omega, -\omega, -\omega)$. The simulations were performed assuming an experimental geometry of parallel polarized beams of wavelengths 2.03 μm and 0.675 μm incident on (100) GaAs (direction of polarization parallel to the $[01\bar{1}]$ crystal axis). Results for the injected carrier density and transmitted third-harmonic (TH) beam are shown in Fig. 9 for the parameters indicated in

TABLE V. Contributions from various (100)-GaAs parameters to the phase-dependent modulation amplitude in carrier density.

| $\text{Re}\chi_3$ ($10^{-19} \text{ m}^2/\text{V}^2$) | $\text{Im}\chi_3$ ($10^{-19} \text{ m}^2/\text{V}^2$) | Length (μm) | Amplitude (%) | Phase offset (rad) |
|--|--|-----------------------------|------------------|-----------------------|
| -7 | -0.7 | 0.20 | 0.048 | 0.51 |
| 0 | -0.7 | 0.20 | 0.028 | 3.3 |
| -7 | 0 | 0.20 | 0.050 | -0.17 |
| -14 | -1.4 | 0.20 | .097 | 0.51 |
| -7 | -0.7 | .002 | 0.12 | 1.7 |
| 0 | -0.7 | .002 | 0.12 | 3.4 |
| -7 | 0 | .002 | 0.017 | 0.0 |

TABLE VI. Contributions from various (111)-GaAs parameters to the phase-dependent modulation amplitude in carrier density.

| $\text{Re}\chi_2$ (10^{-10} m/V) | $\text{Im}\chi_2$ (10^{-11} m/V) | Length (μm) | Amplitude (%) | Phase offset (rad) |
|--|--|-----------------------------|------------------|-----------------------|
| 2.05 | 7.54 | 0.65 | 2.5 | 1.1 |
| 0 | 7.54 | 0.65 | 2.4 | 3.2 |
| 2.05 | 0 | 0.65 | 2.1 | -0.3 |
| 2.05 | 7.54 | 0.006 | 4.7 | 2.1 |
| 0 | 7.54 | 0.006 | 4.7 | 3.3 |
| 2.05 | 0 | 0.006 | 0.2 | 0.0 |

Table IV. Moss *et al.* calculated the effective χ_3 element for this sample orientation to be $-(7. + 0.7i) \times 10^{-19} \text{ m}^2/\text{V}^2$,²⁸ but this input parameter has been doubled for comparison to experimental results (Sec. IV). The small offset between these two traces is due to the small value of $\text{Im}\chi_3$ relative to $\text{Re}\chi_3$. The dependence of this offset on the magnitude of $\text{Im}\chi_3/\text{Re}\chi_3$ is shown in Fig. 10. Comparison to experimental results provides a measurement of $\text{Im}\chi^{(3)}/\text{Re}\chi^{(3)} = 0.11 \pm .03$ in (100) GaAs at $2.03 \mu\text{m}$.

To assess the different contributions to the nonlinear mixing process, various input parameters of the simulation were set to zero and the amplitude of carrier modulation was determined (Table V). The ratio of the cascaded/direct interference contributions was determined to be approximately two to one. The phase offset between the transmitted TH beam and carrier injection was shown to be very sensitive to the presence of the direct interference process. In an extremely thin (2 nm) sample, the direct interference effect dominates. For comparison with experimental results, the simulation was also performed for a value of χ_3 twice that predicted by Moss *et al.*

Though not experimentally realizable, it is interesting to consider the maximum efficacy of carrier control obtained when one- and three-photon absorption rates are balanced. For the wavelengths of $0.83/2.5 \mu\text{m}$, Moss *et al.* predicted a zero value for the $\text{Re}\chi_3$ element and $1.1 \times 10^{-18} \text{ m}^2/\text{V}^2$ for the $\text{Im}\chi_3$ element. For this value of χ_3 and electric-field magnitudes corresponding to balanced one- and three-photon absorption rates, the numerical simulations predicted an efficacy of carrier control greater than 10% with the dominant contribution originating from the direct interference process. The efficacy of density control process increases somewhat beyond 10% if shorter interaction lengths could be used. Unfortunately, the accuracy of these predictions depends on the magnitude of $\text{Im}\chi_5$ (estimated to be $5 \times 10^{-36} \text{ m}^4/\text{V}^4$),²⁷ for which there has been no detailed calculation.

For the 1+2 interference scheme, the relative magnitudes

from the two phase-dependent contributions to carrier injection were also verified by setting various nonlinear coupling terms to zero (Table VI). The numerical results indicate that the quantum interference process strongly affects the carrier injection rate for these experimental parameters. For a very short interaction length (6 nm), the amplitude of control corresponds closely to the ideal case with negligible contribution from the cascaded process, as predicted in Sec. II. Also noted in Table VI is the phase offset between the transmitted SH power and injected carrier density sinusoidal traces. There is a sharp difference in this value for the two different processes. In the cascaded process alone, the change in carrier density closely follows the change in transmitted SH power, indicated by a phase offset close to zero. In the quantum interference process alone, the two traces are nearly out of phase. When both are present, the phase offset falls somewhere between these two extremes. The phase offsets for the very short interaction length match closely the results predicted by the series method solution of the coupled wave equations (as summarized in Table I).

Quantitative experimental results are summarized in Table VII. It should be noted that the value measured for $\Delta N/N$ for the 1+3 studies was limited by experimental sensitivity and the maximum fundamental beam irradiance obtainable. Carrier injection from the one- and three-photon absorption processes was not balanced. As such, the listed value is considered a lower bound for the efficacy of carrier control at these wavelengths and for this experimental geometry.

VI. CONCLUSION

The experimental results for carrier control in GaAs provided an initial verification of the theory of quantum interference control of carrier injection and optical absorption. These studies could be extended to structured materials, as mentioned earlier. This work has explored the use of two different schemes to exploit different material symmetries to obtain interference. Heterostructure engineering could tailor wave function to obtain greater efficacy of control. In any material, quantum interference experiments completed over large wavelength ranges could yield interesting information about the semiconductor that is not accessible through one-beam experiments. Since the interference effect is sensitive to the overlap (and relative phase) of the wave functions involved in the transitions, information can be obtained to assist in mapping out the wave functions of carriers in the crystal. At the very least, these results could be used to verify theoretical calculations of nonlinear susceptibility and band structures. Access to the imaginary component of the nonlinear susceptibility provides a more direct comparison to band-structure calculations than provided by standard experiments

TABLE VII. Experimental results of phase-dependent modulation of carrier density in bulk GaAs.

| Study | GaAs | Wavelengths (μm) | Max $\Delta N/N$ observed (%) | Phase offset (rad) |
|-------|-------|----------------------------------|----------------------------------|-----------------------|
| 1+2 | (111) | 0.775/1.55 | 1.9 | 1.1 |
| 1+3 | (100) | 0.675/2.03 | 0.5 | 0.6 |

which yield the magnitude of the effective tensor element.²⁹

A simple method for verifying theoretical calculations of nonlinear susceptibility terms is suggested by the expression for the maximum contrast obtainable in the modulation of injected carriers. The ratio of modulation to the total number of carriers injected can never exceed a magnitude of unity. This upper bound imposes a relationship between different orders of the nonlinear and linear electric susceptibility tensors. For the 1+2 scheme, the relationship is

$$|\text{Im}[\chi_2^{\text{eff}}(-2\omega; \omega, \omega)]| < \sqrt{\frac{3}{2} \text{Im}[\chi_1^{\text{eff}}(-2\omega; 2\omega)] \text{Im}[\chi_3^{\text{eff}}(-\omega; \omega, \omega, -\omega)]}, \quad (18)$$

where χ_q^{eff} is the effective tensor element, dependent on the polarization of the electric fields. For the 1+3 scheme, a similar inequality holds:

$$|\text{Im}[\chi_3^{\text{eff}}(-3\omega; \omega, \omega, \omega)]| < \sqrt{\frac{10}{3} \text{Im}[\chi_1^{\text{eff}}(-3\omega; 3\omega)] \text{Im}[\chi_5^{\text{eff}}(-\omega; \omega, \omega, \omega, -\omega, -\omega)]}. \quad (19)$$

Thus a lower bound can be calculated for the two-photon absorption of a material from its one-photon absorption coefficient and its second-order nonlinear susceptibility. Likewise, a lower bound for the three-photon absorption can be determined from empirically obtained one-photon absorption measurements and calculations for the third-order nonlinear susceptibility. These inequalities provide a simple method to verify susceptibility calculations or to predict the magnitude of higher-order effects based on the values of lower-order expressions. For example, using the results of Moss *et al.* for $\text{Im}\chi_3^{\text{xxxx}}$, the magnitude of $\text{Im}\chi_5^{\text{xxxxxx}}$ at 0.53 eV must be more than $5.7 \times 10^{-37} \text{ m}^4/\text{V}^4$.

The inequalities of Eqs. (18) and (19) pertain to only the imaginary components of the tensor elements. The real components can be calculated through Kramers-Kronig relationships if the corresponding imaginary part is known over a sufficient wavelength range. Inequalities involving other susceptibility terms can be obtained by consideration of other interference schemes. Inequalities between the tensors of the same order but at different frequencies are also possible. For example, an inequality relating the magnitude of $\text{Im}\chi_3$ at three different wavelengths can be found by consideration of

the maximum fringe contrast in a 2+2 interference scheme (involving three beams of frequencies ω_a , ω_b , and ω_c , where $2\omega_c = \omega_a + \omega_b$).

In conclusion, quantum interference between multiple pathways involving interband transitions in a bulk semiconductor was exploited to dynamically control the rate of free carrier injection and the total optical absorption. Two interference schemes accessed different symmetry properties of the material. Proof-of-principle experiments were conducted in GaAs at room temperature using beams at 1.55/0.775 μm and 2.03/0.675 μm . These coherent control effects should be viewable in a wide range of condensed matter systems.

ACKNOWLEDGMENTS

We are grateful to Tony Springthorpe of Nortel Networks for providing (100)-GaAs samples. We also appreciate many helpful discussions with Ravi Bhat, Daniel Côté, Alain Haché, Anatoli Shkrebti, and John Sipe. Financial support from the Natural Sciences and Engineering Research Council of Canada and Photonics Research Ontario made this research possible. J.M.F. also acknowledges additional support from the Walter C. Sumner Foundation.

*Present address: Institute for Microstructural Sciences, National Research Council Canada, Montreal Road, Ottawa, Ontario, Canada K1A 0R6. Electronic address: james.fraser@nrc.ca

†Electronic address: vandriel@physics.utoronto.ca

¹E.A. Manykin and A.M. Afanas'ev, *Sov. Phys. JETP* **25**, 828 (1967).

²R.J. Gordon and S. Rice, *Annu. Rev. Phys. Chem.* **48**, 601 (1997).

³A.P. Heberle, J.J. Baumberg, and K. Kohler, *Phys. Rev. Lett.* **75**, 2598 (1995).

⁴E. Dupont, P.B. Corkum, H.C. Liu, M. Buchanan, and Z.R. Wasilewski, *Phys. Rev. Lett.* **74**, 3596 (1995).

⁵M. Shapiro and P. Brumer, *J. Chem. Soc., Faraday Trans.* **93**, 1263 (1997).

⁶H. Rabitz, R. de Vivie-Riedle, M. Motzkus, and K. Kompa, *Science* **288**, 824 (2000).

⁷R. Atanasov, A. Haché, J.L.P. Hughes, H.M. van Driel, and J.E.

Sipe, *Phys. Rev. Lett.* **76**, 1703 (1996).

⁸A. Haché, Y. Kostoulas, R. Atanasov, J.L.P. Hughes, J.E. Sipe, and H.M. van Driel, *Phys. Rev. Lett.* **78**, 306 (1997).

⁹J.M. Fraser, A.I. Shkrebti, J.E. Sipe, and H.M. van Driel, *Phys. Rev. Lett.* **83**, 4192 (1999).

¹⁰C. Aversa and J.E. Sipe, *Phys. Rev. B* **52**, 14 636 (1995).

¹¹W. Kohn and J.M. Luttinger, *Phys. Rev.* **108**, 590 (1957).

¹²F.H.M. Faisal, *Theory of Multiphoton Processes*, 1st ed. (Plenum, New York, 1987).

¹³N.W. Ashcroft and N.D. Mermin, *Solid State Physics*, 1st ed. (Saunders College, Orlando, FL, 1976).

¹⁴R. Loudon, *The Quantum Theory of Light*, 2nd ed. (Oxford University Press, U.K. Oxford, 1983).

¹⁵This is correct to within a phase factor. For expressions such as Eq. (7), these phase factors cancel.

¹⁶A. Haché, J.E. Sipe, and H.M. van Driel, *IEEE J. Quantum Electron.* **34**, 1144 (1998).

- ¹⁷J.M. Fraser, A. Haché, A.I. Shkrebtii, J.E. Sipe, and H.M. van Driel, *Appl. Phys. Lett.* **74**, 2014 (1999).
- ¹⁸D. Côté, J.M. Fraser, M. DeCamp, P.H. Bucksbaum, and H.M. van Driel, *Appl. Phys. Lett.* **75**, 3959 (1999).
- ¹⁹M.K. Reed and M.K.S. Shepard, *IEEE J. Quantum Electron.* **32**, 1273 (1996).
- ²⁰J.M. Fraser and K.C. Hall, *Opt. Express* **5**, 21 (1999).
- ²¹Phase-dependent carrier injection for a given interaction length estimated by integrating coupled wave equations including phase mismatch but assuming negligible pump depletion (except for linear absorption) and ignoring multiple reflections. Zero pump depletion uncouples the nonlinear equations. A more accurate estimate could have been obtained using the numerical model but this had not yet been coded.
- ²²E.D. Palik, *Handbook of Optical Constants of Solids*, 1st ed. (Academic, Orlando, FL, 1985).
- ²³Reflection of the optical probe also allowed measurement of injected carrier densities, but this method was determined to be not as sensitive as the technique used.
- ²⁴The presence of carriers does cause other changes to the transmission of an optical probe, including free-carrier absorption and band-gap renormalization. For the probe wavelengths used here, state-filling dominated [Ref. 26].
- ²⁵P. Langot, R. Tommasi, and F. Vallée, *Phys. Rev. B* **54**, 1775 (1996).
- ²⁶B.R. Bennett, R.A. Soref, and J.A. del Alamo, *IEEE J. Quantum Electron.* **26**, 113 (1990).
- ²⁷B.S. Wherrett, *J. Opt. Soc. Am. B* **1**, 67 (1984).
- ²⁸D.J. Moss, E. Ghahramani, and J.E. Sipe, *Phys. Status Solidi B* **164**, 587 (1991).
- ²⁹J.L.P. Hughes and J.E. Sipe, *Phys. Rev. B* **53**, 10 751 (1996).